# Nitrogen-Doped Ti₃C₂ MXene: Mechanism Investigation and Electrochemical Analysis

*Chengjie Lu, Li Yang, Bingzhen Yan, Liangbo Sun, Peigen Zhang, Wei Zhang,\* and ZhengMing Sun\**

Nitrogen doping has been proven to be a facile modification strategy to improve the electrochemical performance of 2D MXenes, a group of promising candidates for energy storage applications. However, the underlying mechanisms, especially the positions of nitrogen dopants, and its effect on the electrical properties of MXenes, are still largely unexplored. Herein, a comprehensive study is carried out to disclose the nitrogen doping mechanism in Ti₃C₂ MXene, by employing theoretical simulation and experimental characterization. Three possible sites are found in Ti₃C₂Tₓ (T = F, OH, and O) to accommodate the nitrogen dopants: lattice substitution (for carbon), function substitution (for –OH), and surface absorption (on –O). Moreover, electrochemical test results confirm that all the three kinds of nitrogen dopants are favorable for improving the specific capacitance of the Ti₃C₂ electrode, and the underlying factors are successfully distinguished. By revealing the nitrogen doping mechanisms in Ti₃C₂ MXene, this work provides theoretical guidelines for modulating the electrochemical properties of MXene materials for energy storage applications.

## 1. Introduction

Chemical doping with heteroatoms is an effective approach to improve the electrochemical performance of many 2D materials (graphene,[1] boron nitride,[2] and molybdenum disulfide[3]) by manipulating their electron transportation process. One of the most investigated examples is nitrogen-doped graphene,[4] the nitrogen-associated defects could transform the inert lattice carbon into an electrochemically active substance, which bring robust redox reactions without affecting the electrical conductivity.[5] Both experimental[6] and theoretical[7] studies have been carried out to reveal the nitrogen-associated defect mechanisms, three main bonding configurations for nitrogen

dopants have been identified within the carbon lattice in graphene, including pyridinic N, pyrrolic N, and quaternary N.[8] In addition, The nitrogen dopants are also found to efficiently induce the transition of Fermi level of graphene[9] and promote the surface wettability,[10] thereby favoring the electrochemical performance of this material.

Inspired by the element doping mechanism of graphene, nitrogen doping has also been employed as a facile strategy to tailor the electrochemical properties of MXenes. The MXenes are generally derived from MAX phases by selectively etching of "A" layer using hydrofluoric acid or other fluorine source treatments, resulting graphene-like monolayer nanostructures. A general formula "$M_{n+1}X_nT_x$" could be used to describe the MXenes, in which M stands for early transition metal, X stands for C and/or N, $T_x$ refers to the functional groups that are introduced as the surface termination during the etching process, generally including –F, –OH, and –O, and $n$ values from 1 to 3.[11] As a novel family of 2D materials, MXene possesses high electrical conductivity, remarkable chemical durability, and intrinsic hydrophilic property, emerging as a promising material for energy storage applications.[12]

As a typical member of the MXene family, $Ti_3C_2T_x$ has been extensively studied for its electrical conductivity and chemical stability.[13] However, the electrochemical performance of the raw $Ti_3C_2T_x$ MXene is not that satisfying.[14] Nitrogen doping has been applied to promote its practical applications.[15] For example, thermal annealing using melamine at high temperature was used to introduce the heteroatom nitrogen into the $Ti_3C_2T_x$ frameworks.[16] The nitrogen-doped $Ti_3C_2T_x$ MXene possesses high surface area and large pore volume, showing outstanding electrochemical performances for lithium–sulfur battery applications. In the analysis of nitrogen existing form, "pyrrolic N," "pyridinic N," and "Ti–N" are quoted to refer to the assigned peaks, of which the concept is "borrowed" from graphene.[17] A similar study was carried out by annealing in ammonia atmosphere to obtain nitrogen-doped MXenes for supercapacitors.[18] An apparent increase in the interlayer spacing was identified after the treatment, ascribed to be the major contribution accounting for the improved specific capacitance. While in the analysis of locations of nitrogen atoms, the three peaks labeled by "N-I," "N-II," and "N-III" were

Dr. C. Lu, Dr. L. Yang, B. Yan, Prof. P. Zhang, Prof. W. Zhang,
Prof. Z. M. Sun
School of Materials Science and Engineering
Southeast University
Nanjing 211189, P. R. China
E-mail: w69zhang@seu.edu.cn; zmsun@seu.edu.cn
Dr. L. Sun
Center of Analysis and Measurement
Harbin Institute of Technology
Harbin 150001, P. R. China
The ORCID identification number(s) for the author(s) of this article can be found under https://doi.org/10.1002/adfm.202000852.

ADVANCED
SCIENCE NEWS
www.advancedsciencenews.com

ADVANCED
FUNCTIONAL
MATERIALS
www.afm-journal.de

believed to originate from Ti−N bond, Ti−O−N bond, and chemisorbed $\gamma$-N$_2$, respectively.[19] Other strategies including hydrothermal[20] and solvothermal[21] treatments are proved to be effective to realize the nitrogen doping process as well. Even though nitrogen doping has been widely investigated to boost the electrochemical performance of the MXene materials, the underlying mechanisms are still in controversy, especially over the existing form of the nitrogen dopants. Moreover, it is ambiguous how nitrogen dopants at different positions affect the electrochemical performance of the MXenes. Theoretical simulation is a convenient and promising technique in mechanism study.[22] However, the relating work on nitrogen-doped MXenes has not yet been reported in literature.

Herein, we investigated the nitrogen doping mechanisms of Ti$_3$C$_2$ MXene through density functional theory (DFT) simulation. By comparing the formation energies of all possible configurations, three energetically favorable sites were determined in Ti$_3$C$_2$T$_x$ modes to accommodate the nitrogen dopants: lattice substitution (LS) for carbon, function substitution (FS) for −OH, and surface absorption (SA) on the −O termination. Correspondingly, three N-Ti$_3$C$_2$ MXenes with nitrogen dopants locating at expected sites were designed and synthesized using different nitrogen doping strategies. The present work reveals the nitrogen doping mechanisms in Ti$_3$C$_2$ MXene, thereby providing theoretical guidelines for manipulating this material for energy storage applications. In addition, the research method and calculation model are also applicable for element doping in other 2D materials.

## 2. Results and Discussion

### 2.1. Simulation of the Nitrogen Dopants in Ti$_3$C$_2$ MXene

DFT simulation has been performed to reveal the nitrogen doping mechanisms in Ti$_3$C$_2$ MXene, which has the chemistry formula of Ti$_3$C$_2$[(OH)$_x$O$_y$F$_z$].[23] Three unitcells, Ti$_3$C$_2$F$_2$, Ti$_3$C$_2$(OH)$_2$, and Ti$_3$C$_2$O$_2$, are optimized, and then the functional groups found their energetically favorable sites during the relaxation process. The obtained lattice parameters, as well as the fraction coordinates of the functional groups, are given in Table S1 in the Supporting Information. The results suggest that the lattice parameter $a$ varies in these three unitcells, ranging from 3.04 to 3.09 Å, well consistent with the data reported in other works.[24]

The nitrogen atoms are simulated to exist mainly as the lattice substitutions in the literature, contributing to the formation of Ti$_3$(C$_{2-\alpha}$, N$_\alpha$)T$_x$ phase, for its foreseeable structural stability. In this work, all the possibilities of lattice substitution, function substitution, and surface adsorption are evaluated from energy, electron, and vibration aspects. In the substitution cases at lattice and function sites, there is only one configuration for each model to accommodate the nitrogen atom, while in the last case of surface absorption, a few possibilities should be considered, such as Ti hollow, C hollow, and T top. An atomic scheme illustrating all the possible configurations of nitrogen dopants in a Ti$_3$C$_2$T$_x$ (T = F, O, and OH) supercell is shown in **Figure 1**a. Then, the formation energy $E_f$ of each configuration is calculated by measuring the energy difference

before and after nitrogen incorporation. The obtained results are displayed in Figure 1b, with the center area in shade referring to positive values. It is found that the formation energy varies with the functional groups in the case of lattice substitution, from −1.31 eV in Ti$_3$C$_2$O$_2$ to −0.09 eV in Ti$_3$C$_2$(OH)$_2$. In other words, the Ti−C bond strength in Ti$_3$C$_2$ MXene can be also affected by the functional groups outside, which could be ordered: Ti$_3$C$_2$(OH)$_2$ > Ti$_3$C$_2$F$_2$ > Ti$_3$C$_2$O$_2$. When it comes to the substitution for functional groups, that for −OH group is found to be most energetically favorable, with the formation energy of −4.71 eV, followed by that for −F group (−3.84 eV). Considering the positive formation energy of 0.02 eV for −O group, the corresponding substitution process is believed to be infeasible. In the last case of surface adsorption, the −O functional group is found to be more suitable for adsorbing nitrogen atoms than the other two functional groups because of the lower formation energy at all sites. In addition, the most energetically favorable site is found at Ti–O mid position, which is obtained by fully relaxation when the N atom is placed at O top, with the formation energy of −2.87 eV on the surface of Ti$_3$C$_2$O$_2$. In conclusion, there are three possible configurations in Ti$_3$C$_2$ MXene to accommodate the nitrogen dopants: lattice substitution for carbon, function substitution for −OH, and surface absorption on the −O termination, with the formation energies of −1.31, −4.71, and −2.87 eV, respectively. The corresponding atomic scheme (from top view) of the N-Ti$_3$C$_2$ MXene with the most energetic configurations is displayed in Figure 1c. It is worthwhile pointing out that in general cases, the model with the lowest formation energy is predicted to be most likely to form in DFT simulation. However, the transition states of these three configurations are different, making it hard to decide which nitrogen dopants dominate merely based on the values of formation energy. Then, the transition states, namely, lattice carbon vacancy for LS, functional group −OH vacancy for FS, and the nitrogen absorbed on surface at energetically unfavorable sites for SA, are studied. The energies required to overcome the transition states are given in Figure 1d. The results suggest that the formation of carbon vacancies in Ti$_3$C$_2$ MXene is most difficult, with an extremely large activation energy of 10.25 eV. Then, the formation of −OH functional group vacancy follows, of which the formation energy is measured to be 4.23 eV. Finally, the absorption of nitrogen atoms on surface turns out to be feasible, since the formation energies at most locations are negative.

### 2.2. Effect of Nitrogen Dopants on the Properties of Ti$_3$C$_2$ MXene

The effect of nitrogen incorporation on the electronic and vibrational properties of Ti$_3$C$_2$T$_x$ has been predicted by computing the density of states of electrons and phonons. Ti$_3$C$_2$O$_2$ is taken as the study model, as the three nitrogen doping types of lattice substitution, function substitution, and surface absorption are possible in Ti$_3$C$_2$O$_2$, while only the former two types exist in the other two Ti$_3$C$_2$T$_x$ (T = F, OH) according to our previous energy calculation. A mixed bonding characteristic in Ti$_3$C$_2$O$_2$ can be determined from **Figure 2**a, that the peak at around −10 eV is mainly composed of Ti 3d and C 2s orbitals, and the peaks below Fermi level (from −6 to −1 eV) represent the hybridization
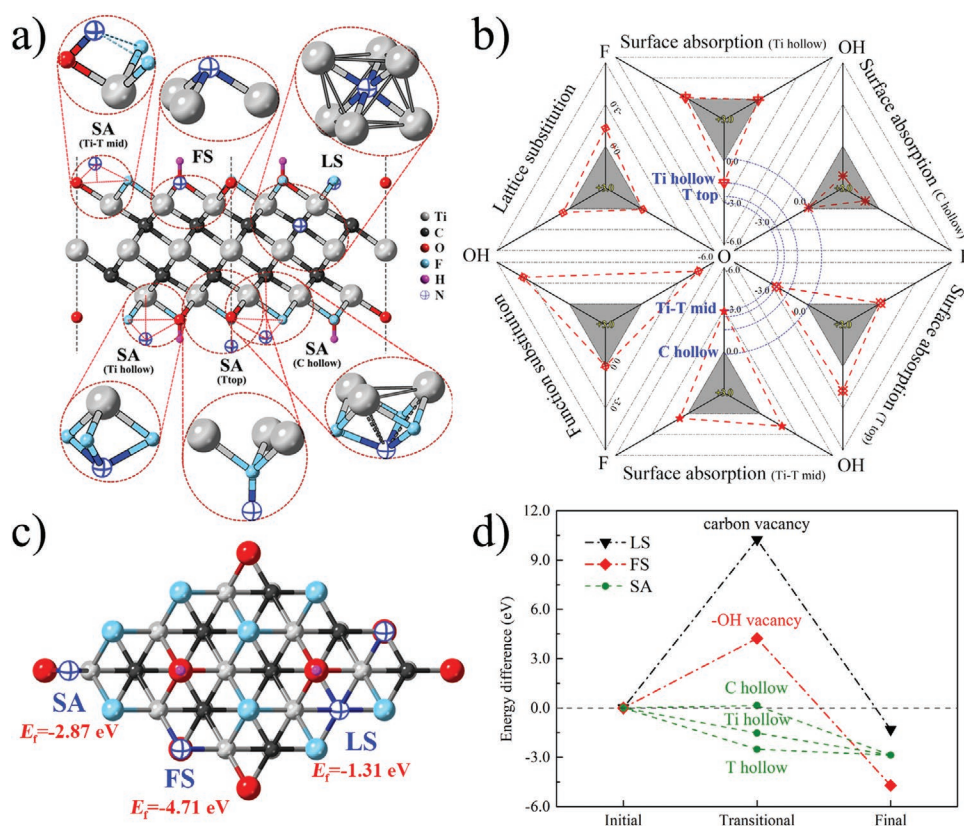
**Figure 1.** Simulation of nitrogen dopants in Ti$_3$C$_2$: a) atomic scheme of Ti$_3$C$_2$T$_x$ with all possible sites for nitrogen dopants; b) formation energy calculation results (shaded part for positive values); c) atomic scheme (top view) of Ti$_3$C$_2$ supercell with nitrogen atoms at the most energetically favorable sites; d) transition state energy calculation results.

of Ti 3d, C 2p, and O 2p orbitals. In addition, the electrons at Fermi level in Ti$_3$C$_2$O$_2$ are mainly contributed by Ti element, suggesting a significant role the Ti—Ti metallic bond plays in conducting electrons. After introducing the dopants into LS and FS sites, the nitrogen atom exhibits a similar bonding feature with the substituted carbon or oxygen atoms according to the magnified partial density of states (PDOS) curves of N element shown in the inset. Therefore, the broken bond is predicted to be reconstructed during the substitution process, bringing limited influence on the stability of Ti$_3$C$_2$O$_2$. When it comes to the last case of SA, an isolated peak originating from the hybridization of Ti 3d, C 2p, and N 2p orbitals can be found at around Fermi level, which suggests an enhanced Ti—Ti metallic bond. This phenomenon might be attributed to a weakened hindrance from functional groups with the absorption of nitrogen atoms on the surface. In consequence, the nitrogen absorbed on surface contributes to the formation of Ti—O—N bond, endows the Ti$_3$C$_2$O$_2$ MXene with improved conductivity.

According to the vibration density of states curves of Ti$_3$C$_2$O$_2$ shown in Figure 2a, a hybrid bonding feature can be also identified. The peaks between 14 and 22 THz represent the strong Ti—C and Ti—O covalent bonds. In addition, the sympathetic vibration mode between 9 to 14 THz originates from a weakened Ti—C bond, which is not discovered in its precursor Ti$_3$AlC$_2$ phase. Therefore, the Ti—C bond is also weakened with the elimination of Al atoms. The states below 9 THz are generally contributed by Ti atoms, suggesting a weak Ti—Ti metallic

bond. When the nitrogen atom is introduced at the lattice site, the vibration density of states (VDOS) curves of Ti$_3$(C, N)$_2$O$_2$ are shown in Figure 2b. It is observed that the nitrogen atom mainly forms the strong covalent bond with Ti atoms, and the model is found to be stable in the vibration aspect, without any states locating below Γ point. In the case of forming FS model, the obtained VDOS curves are displayed in Figure 2c. The substitution behavior brings no imaginary vibration modes at negative frequency, suggesting that the Ti$_3$C$_2$(N,O)$_2$ model exhibits excellent structural stability. Moreover, the vibrational mode of −N functional group is similar with that of −O, forming a strong covalent bond (peaks around 15 THz) and a relatively weak one (peaks around 4 THz) with Ti element. Considering that a similar vibrational model at low frequency part in Ti—O bond is located at around 12 THz, the Ti—N bonding strength is deduced to be much weaker. This conclusion is in well consistence with the formation energy calculations that the −O termination is more energetically favorable than −N. When it comes to the SA model, the vibration density of state shown in Figure 2d indicates that the nitrogen atom is unstable, mainly due to the vibration mode along basal plane. However, such unstable vibrational behaviors are expected to be stabilized when the nitrogen content is high. Apart from the imaginary part, the nitrogen atom also forms a strong covalent bond with −O termination, and a mixed bond with Ti atoms, deduced according to the vibration modes at around 30 and 12 THz, respectively. Although the formation of Ti—O—N bond on the MXene surface is concluded
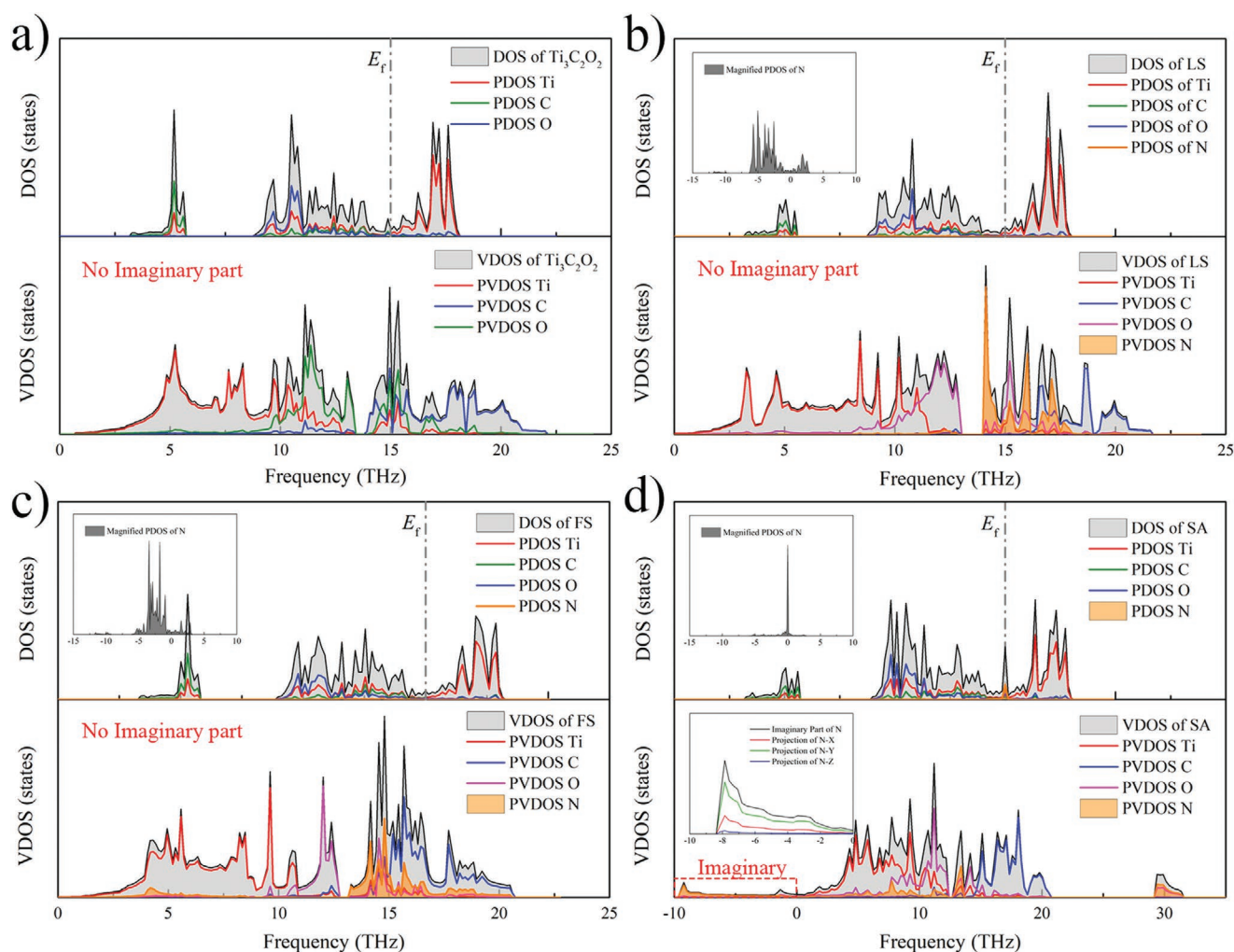
**ADVANCED
SCIENCE NEWS**

www.advancedsciencenews.com

**ADVANCED
FUNCTIONAL
MATERIALS**

www.afm-journal.de

**Figure 2.** The computed electron density of states (DOS) and vibration (phonon) density of states (VDOS) of: a) $Ti_3C_2O_2$; b) LS; c) FS; d) SA (with inset figures for magnified PDOS of nitrogen, and imaginary partial vibration density of states of nitrogen projected along $x$, $y$, and $z$ axes when unstable).

in previous electron analysis, it is unexpected that the doped nitrogen atoms form strong bonds with Ti atoms and –O terminations, suggesting a strong chemical interaction instead of a weak physical absorption in the case of SA.

### 2.3. Fabrication of Nitrogen-Doped $Ti_3C_2$ MXenes

According to the DFT simulation, three possible sites are determined in $Ti_3C_2$ MXene to accommodate the nitrogen dopants: lattice substitution, function substitution, and surface absorption. Correspondingly, three N-$Ti_3C_2$ MXenes are synthesized, with nitrogen dopants locating at these three different sites. $Ti_3CN$ MXene is prepared by in situ etching from $Ti_3AlCN$, with nitrogen atoms definitely locating at carbon lattice site. Although it is reported that a high temperature annealing (above 500 °C) in ammonia favors the transformation from $Ti_3C_2$ to $Ti_3CN$, decomposition product (TiN) is found after the treatment.[18] According to the previous transition states analysis, the nitrogen substitution for –OH functional group is easier than that for lattice carbon. Therefore, an intermediate

temperature treatment might be feasible to realize this process. The hydrothermal (around 200 °C) method is adopted to treat the pristine $Ti_3C_2$ MXene, labeled as HND in this work. Finally, the cold plasma technique, which is anhydrous, conducted at low vacuum and low temperature (lower than 100 °C), is carried out to introduce nitrogen atoms onto the surface of pristine $Ti_3C_2$ MXene, labeled as PND in this work.

The four MXenes, the pristine and the three N-doped, were investigated using scanning electron microscope (SEM), and the element distribution was analyzed by energy-dispersive spectrometer (EDS) mapping, as displayed in **Figure 3**. It is found that the size of the pristine $Ti_3C_2$ particle is around 10 µm. In the case of $Ti_3CN$, a representative accordion-like morphology can be clearly observed, with a much smaller particle size of around 6 µm. For HND, particles with fewer layers and thinner thickness can be determined, and the size also turns to be smaller (7 µm), because $Ti_3C_2$ MXene might be fragmentized with the vaporization process during the hydrothermal treatment at high temperature. The morphology of PND suggests that the particle size generally remains unchanged after the cold plasma treatment. In the EDS mapping as shown in Figure 3b,
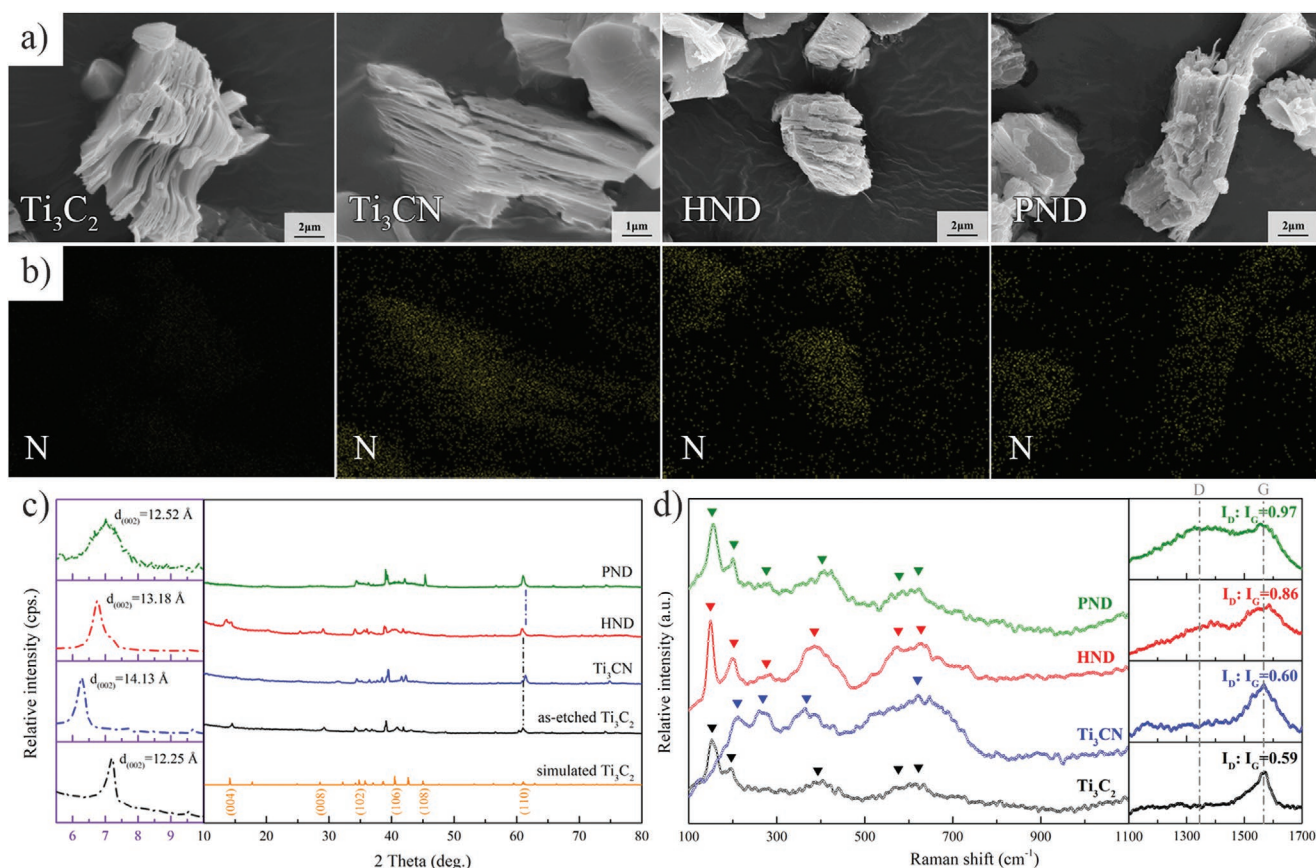
**Figure 3.** Characterization of the MXenes: a) SEM morphology of the pristine $Ti_3C_2$, $Ti_3CN$, HND, and PND MXenes; b) element distribution (EDS mapping) of nitrogen element; c) XRD patterns; d) Raman spectra.

the distribution pattern of nitrogen element can be clearly identified in N-$Ti_3C_2$ MXenes, which is also in consistence with Ti, oxygen, and fluorine elements as shown in Figures S1–S4 in the Supporting Information. It can be concluded that the nitrogen dopants have been successfully introduced using the hydrothermal and cold plasma treatment. The nitrogen content in $Ti_3CN$ is primarily determined by measuring the ratio of C:N in $Ti_3CN$, which is about 4:1. Correspondingly, the chemical formula of could be expressed by $Ti_3(C_{1.6}, N_{0.4})$.

The interlayer spacing of the four different MXenes (pristine, $Ti_3CN$, HND, and PND) was then measured with X-ray diffraction (XRD) spectra (Figure 3c), together with a simulated pattern from $Ti_3C_2O_2$ model (lattice $a$ = 3.04 Å; lattice $c$ = 25.0 Å). It is obvious that the patterns of pristine $Ti_3C_2$ and the simulated model are consistent, with typical peaks distributing at 7.2°, 14.5°, 29.8°, and 61.0°, which originate from the diffraction of (002), (004), (008), and (110) planes, respectively. The lattice $a$ and interlayer spacing $c/2$ of the as-etched $Ti_3C_2$ MXene are calculated to be 3.04 and 12.25 Å, respectively. In the magnified low angle area, the peak representing the diffraction from (002) plane is discovered to shift toward low angle with the presence of nitrogen dopants in the cases of $Ti_3CN$ and HND. Correspondingly, the interlayer spacing of these two MXenes is determined to be 14.13 and 13.18 Å, respectively. Moreover, the peak representing the diffraction from (110) plane remains unchanged in the cases of HND and PND, but slightly shifts to

higher angle of 61.4° in $Ti_3CN$. Therefore, the function substitution and surface absorption nitrogen atoms possess limited effect on lattice $a$, while in the case of lattice substitution, the value decreases to 3.01 Å. This is also proved in the DFT simulation that the substitution of nitrogen for carbon would lead to a decline in lattice parameters, from 3.04 Å in $Ti_3C_2O_2$ to 3.02 Å in $Ti_3CNO_2$, and from 3.08 Å in $Ti_3AlC_2$ to 3.05 Å in $Ti_3AlCN$.

Figure 3d shows the Raman spectra of the four MXenes, with typical peaks of $Ti_3C_2$ locating at 198, 266, 386, 579, and 620 cm⁻¹, respectively.[25] In addition, there are two broad peaks located between 1200 and 1800 cm⁻¹, which are characteristic for the D- and G-modes of graphitic carbon: the former D-band is generally related with the disordered graphite formed by the defects in carbon-based materials, while the latter G-band is assigned to the stacking of the graphite hexagon network plane.[26] It can be seen that the ratios of $I_D$:$I_G$ in $Ti_3C_2$ and $Ti_3CN$ MXenes are relatively close, with the values of 0.59 and 0.60. When it comes to the cases of HND and PND, a remarkable rise in the intensity of D-band can be observed, contributing to a larger ratio of $I_D$:$I_G$ up to 0.86 and 0.97, respectively. Therefore, the hydrothermal and cold plasma treatment promote the formation of thinner nanosheets with more defects (e.g., porosity and broken nanosheets),[27] which is well in line with the SEM results. Finally, the surface microstructure is also a very important parameter affecting the properties of MXene materials, which is evaluated by zeta potential test and wetting

experiments. A detailed description can be found in Figures S5 and S6 in the Supporting Information. It is concluded that the wettability of MXene electrodes is generally improved with the introduction of nitrogen dopants, and the surface polarity can be also significantly affected.

## 2.4. Characterization of the Nitrogen Dopants in Ti$_3$C$_2$ MXene

DFT simulation is capable of computing the charge distribution, according to which the charge transfer could be precisely determined using Bader analysis. The elemental valence state is important in the study of MXene materials, according to which the energy required to active the in-core electrons can be determined (the more valence electrons the atom has, the weaker constraining force the core has to its electrons). This analysis method accords with the underlying principles of X-ray photoelectron spectroscopy (XPS) characterization, thereby providing theoretical foundations in the understanding of XPS results. It is noted that in literature the peaks in XPS spectra are generally assigned by bonding type, which is another representation of valence state.[28] However, this method has been proved to be incomprehensive in some examples like graphene, as the binding energy of N 1s varies with the existing forms despite of the same bonding type (C−N bond).

The valence state analysis of carbon, nitrogen, oxygen, and titanium elements in Ti$_3$C$_2$ MXenes are displayed in **Figure 4**a. It can be seen that the introduction of nitrogen dopants has different impacts on the valence states of each elements. In the case of carbon, Ti$_3$C$_2$T$_x$ MXene terminated with fluorine (T = F) possesses the most electrons, followed by Ti$_3$C$_2$(OH)$_2$ and Ti$_3$C$_2$O$_2$, with the valence states of $V_C^F = -1.79$, $V_C^{OH} = -1.77$, and $V_C^O = -1.65$, respectively. After introducing nitrogen dopants, a new valence state of $V_C^N = -1.52$ presents in FS, while the valence state of carbon element remains generally unchanged in the other two cases. The valence states of nitrogen element turn out to be distinguishing when distributed at different sites: the doping nitrogen atom at lattice site possesses the most electrons, followed by that at function site, with the values of $V_N^{LS} = -1.59$ and $V_N^{FS} = -1.37$, respectively. When adsorbed on the surface, the valence state varies with the form, $V_N^{SA} = -0.07$ in [N], and $V_N^{SA} = -0.43$ in [NH], while in the latter case the extra electrons are provided by hydrogen. Similar result is obtained in the case of oxygen: the valence state of oxygen in Ti$_3$C$_2$(OH)$_2$ is $V_O^{OH} = -1.31$, while that in Ti$_3$C$_2$O$_2$ is $V_O^O = -1.09$. With the introduction of nitrogen dopants, the valence states remain unchanged in the cases of LS and FS, but decreased to $V_O^{SA} = -0.85$ in SA. When it comes to Ti element, two valence states are found: the inner Ti atom constructs the TiC octahedron with 2 carbon atoms, with a valence state of



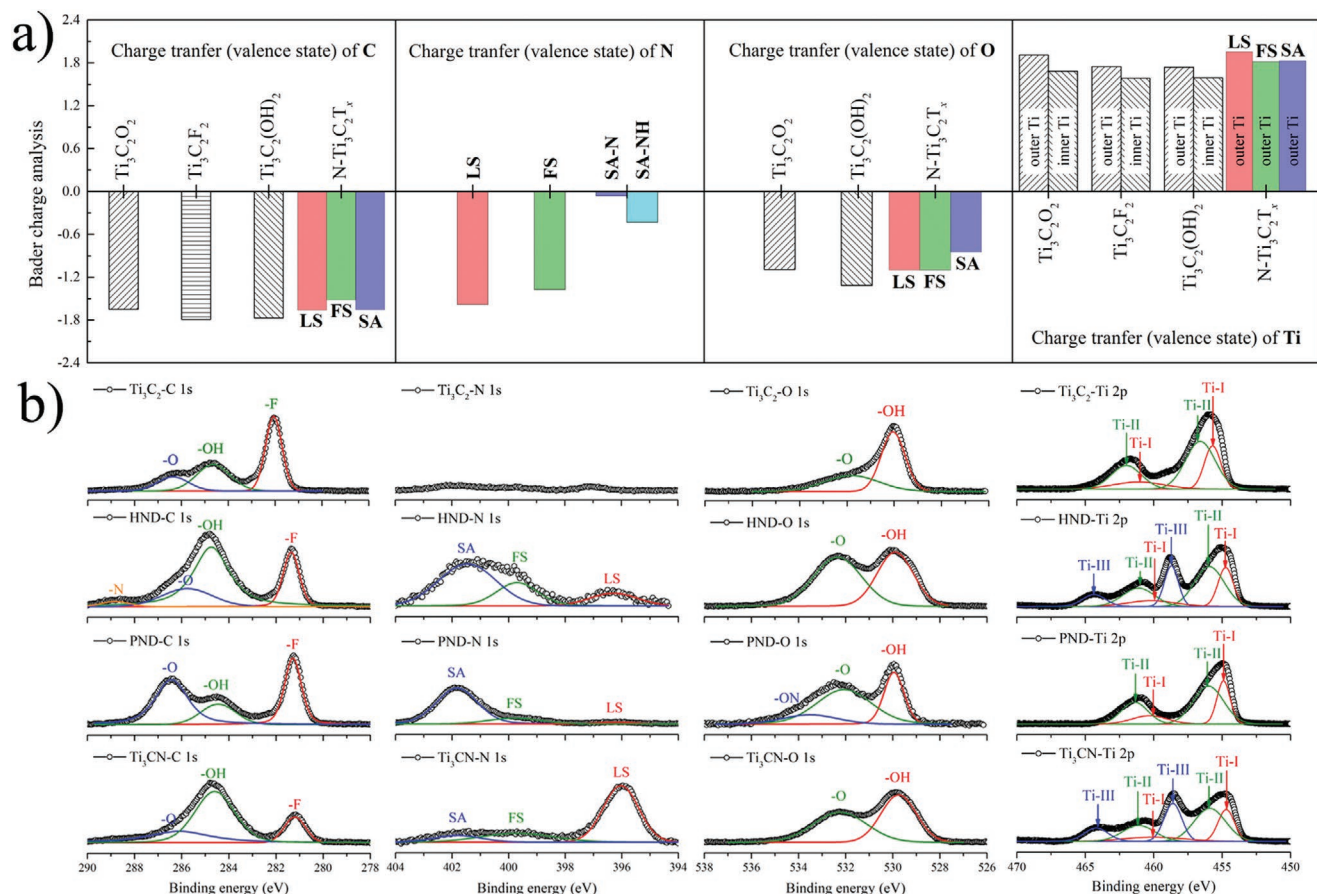**Figure 4.** Characterization of the nitrogen dopants in the N-Ti$_3$C$_2$ MXenes: a) Bader charge analysis (valence state) of carbon, nitrogen, oxygen, and titanium elements; b) XPS spectra of the pristine Ti$_3$C$_2$, HND, PND, and Ti$_3$CN MXenes.

**ADVANCED
SCIENCE NEWS**
www.advancedsciencenews.com

**ADVANCED
FUNCTIONAL
MATERIALS**
www.afm-journal.de

$V_{i-Ti} = +1.63$ on average. The other 2 equivalent Ti atoms, marked as outer Ti, possesses a higher valence state of $V_{o-Ti}^O = +1.91$ when terminated with –O, and a lower valence state of $V_{o-Ti}^{F/OH} = +1.74$ when terminated with –F and –OH. With the introduction of nitrogen dopants, the valence state of outer Ti increases to $V_{o-Ti}^{LS} = +1.95$ in the case of LS, and decreases by 0.1 in the cases of FS and SA, while that of inner Ti generally remains unchanged. Since the change in the valence state of titanium, oxygen, and nitrogen elements is strongly correlated with the redox reaction during the charge/discharge process,[29] it is deduced that the introduced nitrogen dopants would affect the electrochemical performance of $Ti_3C_2$ MXene, which will be further discussed in following sections.

A combined analysis based on Bader charge simulation and XPS characterization is primarily conducted in a simple system, the pristine $Ti_3C_2$ MXene. The two carbon atoms in each $Ti_3C_2T_x$ model should be equivalent. Therefore, the three peaks found in Figure 4b should be attributed to their different valence states, originating from the functional groups outside: peak I at 282.1 eV, peak II at 284.6 eV, and peak III at 286.4 eV represent the functional groups of –F ($V_C^F = -1.79$), –OH ($V_C^{OH} = -1.77$) and –O ($V_C^O = -1.65$), respectively. In addition, the proportion of each functional group can be determined by integrating the peak area, making the pristine $Ti_3C_2$ MXene possess a chemical formula of $Ti_3C_2[F_{0.46}(OH)_{0.35}O_{0.19}]$. Similarly, in the case of oxygen element, the peak I at 530.1 eV stands for –OH ($V_O^{OH} = -1.31$), and peak II at 531.8 eV stands for –O ($V_O^O = -1.09$). When it comes to the Ti element, the peak assignment is complicated, with some principles to follow. Taking the pristine $Ti_3C_2$ MXene for example: there exists a fixed ratio of 2:1 for Ti 2p (3/2) to Ti 2p (1/2), along with a fixed doublet separation (5.4 eV in this work). It can be seen that the peak I at 455.6 eV refers to the inner Ti element ($V_{i-Ti} = +1.63$), while the other widened peak II at 456.5 eV refers to the outer Ti element ($V_{o-Ti}^O = +1.91$ and $V_{o-Ti}^{F/OH} = +1.74$), with an area ratio of Ti-I:Ti-II = 1:2. In the case of HND, a new couple of peaks III (Ti 3p/2 and Ti p/2) appear at 458.8 and 464.2 eV, respectively, which are deduced to come from the oxidation product $TiO_2$ formed during the hydrothermal treatment. When it comes to PND, the curve shape of the Ti 2p spectrum is similar with that of $Ti_3C_2$ MXene, suggesting that the oxidation state of Ti element generally remains unchanged. In the last case of $Ti_3CN$, the couple of peak III (Ti 3p/2 and Ti p/2) can be also observed, making the Ti 2p spectrum similar with that of HND. However, this high oxidation state of Ti element (peak III) refers to the Ti atoms bonded with nitrogen at lattice site, as suggested in Figure 4a that the lattice nitrogen substitution endows the Ti atom with a higher oxidation state. In consequence, the oxidation state of Ti element can be arranged as follows: pristine $Ti_3C_2$ = PND < HND (increased with the formation of $TiO_2$) = $Ti_3CN$ (increased with the formation of nitrogen lattice substitution). It is noted that "Ti-C," "Ti$^{2+}$," and "Ti$^{3+}$" are generally quoted during the assignment of Ti element in literature,[30] exactly referring to inner Ti, outer Ti and high-valence-state Ti (oxidized or bonded with nitrogen) in this work. It is worthwhile pointing out that the experiment work conducted by Lukatskaya et al.[31] using in situ X-ray absorption spectroscopy (XAS) revealed that the average Ti oxidation state in $Ti_3C_2T_x$ is much closer to +2 than +4, which is well in line with our calculation results.

The existing form of nitrogen dopants in N-$Ti_3C_2$ MXenes can be understood from the XPS results, together with the DFT calculation. The total survey spectra in Figure S7 in the Supporting Information clearly show the presence of N 1s peak in HND, PND, and $Ti_3CN$, indicating the successful incorporation of nitrogen into the $Ti_3C_2$ layers. The concentration of nitrogen dopants in these three N-$Ti_3C_2$ MXenes is calculated accordingly, determined to be 2.3, 9.1, and 6.1 at%, respectively. According to the high-resolution spectrum of N 1s, three peaks can be identified at around 396.0, 399.7, and 401.9 eV, which are assigned to be N-Ti (nitride), N-5 (pyrrolic nitrogen), and N-Q (quaternary nitrogen) in literature, respectively.[21] The peak at 396.0 eV in the XPS curve of $Ti_3CN$ is originated from the nitrogen at lattice site, which is in consistence with the DFT calculation that the number of valence electrons of nitrogen follows the sequence of: LS ($V_N^{LS} = -1.59$) > FS ($V_N^{FS} = -1.37$) > SA ($V_N^{SA} = -0.43/-0.07$). Therefore, "LS" is marked to refer to the N 1s peak from lattice (substitution) site in this work. Accordingly, the other two peaks locating at around 399.7 and 401.9 eV are marked as "FS" and "SA", originating from –N functional group and [N] surface absorption, respectively. It is reasonable to deduce that the nitrogen dopants introduced by cold plasma technique mainly exist as surface adsorption, due to the low treatment temperature. The above analysis could be confirmed by the analysis of carbon and oxygen elements in the XPS data. The new peak labeled in HND at 288.8 eV illustrates the formation of –N functional group ($V_C^N = -1.52$ for carbon in $Ti_3C_2(O, N)$), and the extra peak presents at 533.5 eV originates from the charge transfer effect when the nitrogen dopants are absorbed on surface ($V_O^{SA} = -0.85$ for oxygen in $Ti_3C_2O_2[N]$). In summary, there are three possible nitrogen species in $Ti_3C_2$ MXene, lattice (substitution) site, function (substitution) site, and surface absorption, corresponding to the three peaks in the N 1s XPS spectrum at 396.0, 399.7, and 401.9 eV, respectively.

## 2.5. Nitrogen-Doped MXene for Supercapacitors

The excellent electrochemical performance of MXene electrodes is generally attributed to the pseudocapacitive energy storage mechanism, and the change in the titanium oxidation state (valence state) is successfully detected by in situ XAS.[29] Although the direct simulation of redox reaction is difficult using DFT method, it is possible to calculate the number of unfilled orbitals of each element, representing the limitation for electron transferring effect during the charge/discharge process. Taking nitrogen, for example, the orbital analysis results are illustrated in **Figure 5**a, which is essentially another representing form of valence state. The highest platform (–1.59) is found in nitrogen at carbon lattice site, suggesting that there are at least 1.41 unfilled orbitals available to accommodate the electrons in each doped nitrogen atom. Therefore, the maximum capacitance contributed by nitrogen through pseudocapacitive mechanism is predicted to be: LS < FS < SA (NH) < SA (N). Figure 5b shows the orbital analysis results of oxygen. It can be seen that there are 0.91 unfilled orbitals existing in the oxygen of $Ti_3C_2O_2$, and decreases to 0.69 in $Ti_3C_2(OH)_2$, which are filled by the electrons from hydrogen. Experimental evidence can be found in literature that there exists a transferring from –O
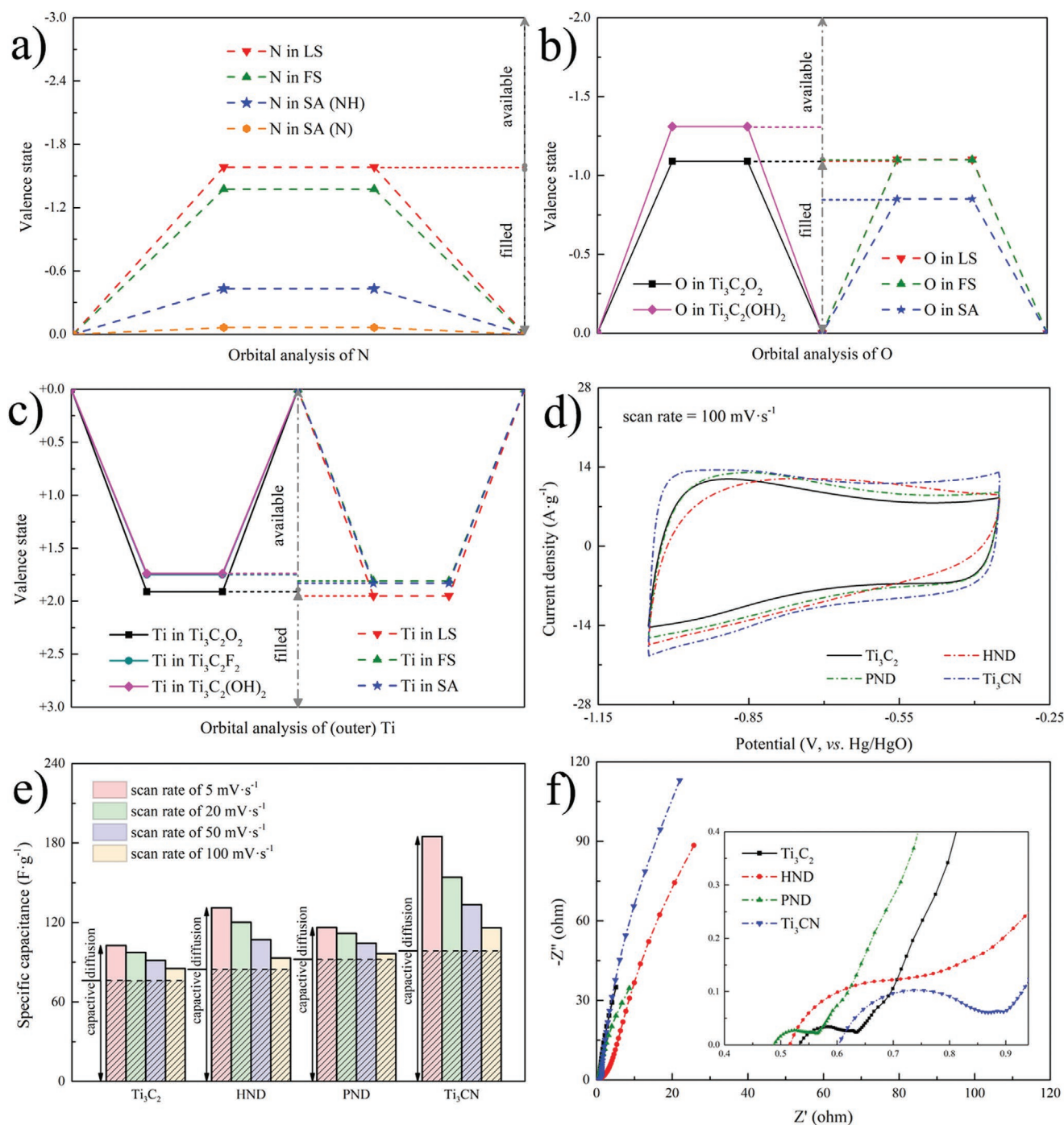
**Figure 5.** Electrochemical performance of the pristine $Ti_3C_2$, HND, PND, and $Ti_3CN$ MXenes: theoretical band analysis (bottom part for filled orbitals, and upper part for unfilled orbitals) of a) nitrogen, b) oxygen, and c) titanium elements. Electrochemical test results of d) CV profiles at 100 mV s$^{-1}$; e) specific capacitances at 5, 20, 50, and 100 mV s$^{-1}$, with the calculated specific contribution from capacitive controlled (bottom part) and diffusion controlled (upper part) behaviors; f) Nyquist plots with the magnified high-frequency region.

termination to –OH during the charging process.[32] Moreover, it is proposed that the –O functional group in $Ti_3C_2$ MXene is more active in the redox reaction than –OH and –F.[33] After introducing nitrogen dopants, more unfilled orbitals can be determined in the oxygen of SA. Consequently, an improved pseudocapacitance (PC) from oxygen can be expected with the

absorption of nitrogen atoms on surface. The valence state of Ti element is also a very important parameter affecting pseudocapacitance, the corresponding orbital analysis results are shown in Figure 5c. It is concluded that the Ti element in $Ti_3C_2O_2$ possesses the most unfilled orbitals, followed by that of $Ti_3C_2(OH)_2$ and $Ti_3C_2F_2$, which suggests that the chemical

**Table 1.** Contributing mechanisms as well as the underlying factors of nitrogen dopants to the total capacitance of N-Ti$_3$C$_2$ MXenes ("GU" for generally unchanged, "SI" for slightly increased, and "RI" for remarkably increased).

| Mechanisms | | Underlying factors | HND | PND | Ti$_3$CN |
|---|---|---|---|---|---|
| Capacitor-like | EDLC | Interlayer spacing | SI | GU | RI |
| | PC | –O functional groups | GU | SI | GU |
| | | –N functional groups | SI | GU | GU |
| | | [N/NH] surface absorption | SI | RI | GU |
| Diffusion-controlled | | Oxidation state of Ti | SI | GU | RI |

activity of Ti element in Ti$_3$C$_2$ MXene is significantly hindered by the –OH and –F functional groups. With the introduction of nitrogen dopants, a slight decrease in the number of unfilled orbitals of Ti element can be found in the cases of FS and SA, together with a slight increase in LS. Accordingly, the contribution from pseudocapacitive mechanism of Ti element can be predicted, following the sequence of: LS > Ti$_3$C$_2$O$_2$ > SA > FS > Ti$_3$C$_2$(OH)$_2$ ≈ Ti$_3$C$_2$F$_2$.

The electrochemical tests are carried out to verify the simulation results. The cyclic voltammetry (CV) behaviors of the four MXene electrodes at the scan rate of 100 mV s$^{-1}$ are displayed in Figure 5d. It is found that the four materials do not exhibit adherent rectangular CV appearance, suggesting a strong contribution from pseudocapacitive mechanism. Since the existing form, as well as the doping content of nitrogen in each electrode is different, it makes little sense to compare the three doping strategies according to specific capacitance integrated from the cycled area of CV curves. Therefore, we focus on revealing the contribution mechanism of each nitrogen species in this work. The current response, $i(V)$, can be usually resolved by two parts: capacitor-like and diffusion-controlled behaviors, following Equation (1)[34]

$$i(V) = k_1 v + k_2 v^{1/2} \tag{1}$$

The factors of $k_1$ and $k_2$ as a function of potential ($V$) can be determined accordingly. The contribution from capacitor-like and diffusion-controlled behaviors is displayed in Figure 5e. The capacitor-like part in each electrode generally remains unchanged with the rising scan rates, suggesting that the degeneration in total specific capacitance at high scan rate mainly originates from a low contribution from diffusion-controlled part. In addition, all the three N-Ti$_3$C$_2$ electrodes are found to have a higher contribution from capacitor-like behavior than the pristine Ti$_3$C$_2$ electrode, with the values increased from 76.1 F g$^{-1}$ in Ti$_3$C$_2$ to 84.6, 92.2, and 98.6 F g$^{-1}$ in HND, PND, and Ti$_3$CN electrodes at the scan rate of 5 mV s$^{-1}$, respectively. The capacitor-like behavior is sensitive to the surface composition, which can be generally divided into two parts: electrical double-layer capacitance (EDLC) relating with the intercalation of hydrated ions between MXene interlayers; PC relating with the redox reaction from surface absorption and functional groups. Combined with simulation and characterization results, the factors contributing to the enhanced capacitor-like performance in each N-Ti$_3$C$_2$ electrode can be distinguished. In the case of HND, an increase in the interlayer spacing is characterized, together with the formation of –N function substitution and [N/NH] surface absorption, suggesting both contributions

from EDLC and PC mechanisms. When it comes to the case of PND, the change in the interlayer spacing after treatment is insignificant. Therefore, the improved part is mainly ascribed to the PC mechanism, originating from the high content of [N/NH] surface absorption, as well as an increased number of unfilled orbitals in –O functional group when forming Ti−O−N bond. While in the Ti$_3$CN electrode, only a remarkable increase in the interlayer spacing is identified, making the EDLC mechanism dominating in the improved capacitance.

Apart from the capacitor-like behavior, the diffusion controlled part is generally related with the redox reaction from bulk elements, in specific, Ti in Ti$_3$C$_2$ MXene. According to the orbital analysis of Ti element shown in Figure 5c, Ti in Ti$_3$C$_2$O$_2$ with nitrogen at carbon lattice site (LS) possesses more unfilled orbitals, followed by that on surface (SA) and at function site (FS). Correspondingly, an apparent contribution from the diffusion-controlled behavior is identified in Ti$_3$CN electrode, follows by HND and PND with the values of 86.4, 46.5, and 24.2 F g$^{-1}$ at the scan rate of 5 mV s$^{-1}$, respectively. It is worthwhile pointing out that the oxidation states of Ti element in FS and SA are close, since the simulation is performed basing on Ti$_3$C$_2$O$_2$ model. However, the –N functional group is simulated to form by substituting for –OH or –F ones, thereby the diffusion controlled behavior in HND is apparently promoted in experiments. As a conclusion, the contribution mechanisms of nitrogen dopants to the total capacitance of N-Ti$_3$C$_2$ MXenes, together with the underlying factors, are summarized in **Table 1**.

The kinetic features of ion diffusion on the four electrodes are investigated using electrochemical impedance spectroscopy, with the obtained Nyquist plots shown in Figure 5f. The equivalent series resistance (ESR) obtained from the intercept of the Nyquist plot with the real axis is donated as $R_s$, which represents the impedance of the electrolyte and electrode.[35] The PND and HND electrodes are found to possess better ion response than Ti$_3$C$_2$, with lower resistance of $R_s = 0.49$ Ω and $R_s = 0.51$ Ω than that of $R_s = 0.53$ Ω. Therefore, the nitrogen dopants existing as –N termination or [N/NH] absorption would decrease the internal resistance of the electrode. Another important parameter, $R_{ct}$, representing the charge transfer resistance at the electrode/solution interface, could be determined by the diameter of the semicircle in the high-frequency region.[36] The charge transfer resistance of HND is measured to be as large as $R_{ct} = 0.32$ Ω, which is mainly attributed to the TiO$_2$ nanoparticles formed during the hydrothermal treatment according to the high solution Ti 2p spectrum of HND. It can be observed that the PND electrode possesses a lower charge transfer resistance ($R_{ct} = 0.08$ Ω) than Ti$_3$C$_2$ ($R_{ct} = 0.10$ Ω), which is in excellent consistence with our previous DFT simulation that the conductivity

**ADVANCED
SCIENCE NEWS**

www.advancedsciencenews.com

**ADVANCED
FUNCTIONAL
MATERIALS**

www.afm-journal.de

of $Ti_3C_2$ MXene might be favored by the nitrogen dopants absorbed on surface. It is interesting to find that although both the values of the equivalent series resistance $R_s$ and charge transfer resistance $R_{ct}$ in $Ti_3CN$ are very large, its low-frequency line is still most subcortical, demonstrating a high contribution from diffusion-controlled part, and cations can easily permeate into the interlayer of the active material.[37]

According to the electrochemical test results, it is concluded that the capacitance of $Ti_3C_2$ and $N-Ti_3C_2$ electrodes generally consists of two parts: the diffusion-controlled behaviors relating with the redox reaction from the bulk elements, is dependent on the oxidation state of Ti element in $Ti_3C_2$ MXene. With the substitution of nitrogen dopants for lattice carbon in $Ti_3C_2$ MXene, the capacitance of this part can be significantly improved; the capacitor like behaviors consists of electrical EDLC and PC, which is strongly affected by interlayer spacing, surface absorption and functional groups. With the substitution of nitrogen atoms at functional sites, as well as the absorption on surface, the capacitance of this part can be significantly improved.

## 3. Conclusions

We have demonstrated three possible sites in $Ti_3C_2$ MXene to accommodate the nitrogen dopants: LS for carbon atoms, FS for –OH functional group, and SA relating with the –O termination, with the formation energy of −1.31, −4.71, and −2.87 eV, respectively. Then, three $N-Ti_3C_2$ MXenes, namely, $Ti_3CN$, HND, and PND, are synthesized using different strategies: in situ etching from $Ti_3AlCN$, hydrothermal treatment and cold plasma technique. The existing forms of nitrogen dopants in the three $N-Ti_3C_2$ MXenes are determined by XPS analysis: the three peaks observed at 396.0, 399.7, and 401.9 eV in the high-resolution spectrum of N 1s belong to the nitrogen atoms at lattice (substitution) site, function (substitution) site, and surface adsorption, respectively. The electrochemical behaviors of the four MXene electrodes suggest that the total capacitance can be divided into two parts: the diffusion-controlled part relating with the redox reaction from the bulk element, mainly dependent on the oxidation state of Ti element in $Ti_3C_2$ MXene, and the capacitor-like part consisting of EDLC and PC mechanisms, which are strongly affected by interlayer spacing, surface absorption, and functional groups.

## 4. Experimental Section

*Material Synthesis*: The $Ti_3C_2$ MXene studied in this work was prepared by etching from its precursor of $Ti_3AlC_2$, using a mixture solution of hydrochloric acid (HCl) and lithium fluoride (LiF).[1] The details of the synthesis process is given as follows: $Ti_3AlC_2$ powders (2.0 g) were slowly added into a solution that was composed of LiF (2.0 g) and HCl (40 mL, 9 mol $L^{-1}$), and then stirred at 40 °C for 24 h. Afterward, the achieved suspension was washed using deionized water for several times, till the pH value reached up to 6. Finally, the $Ti_3C_2$ powders were obtained from the sediment by getting dried in a vacuum oven at 80 °C for 24 h.

Three different strategies were applied to introduce the nitrogen dopants to $Ti_3C_2$ MXene in this work. First, the popular one-step hydrothermal treatment was carried out using reductive urea ($CH_4N_2O$) as the nitrogen source. In addition, the air dissolved in the solution was exhausted by inletting argon to further prevent the oxidation of

$Ti_3C_2$ MXene. A detailed study on the processing parameters could be found in the previous work.[38] Briefly, MXene powders (100 mg) were dissolved in aqueous solution of urea (60 mL, 15 wt%). Afterward, the dispersion was sealed in a Teflon-lined autoclave, and then installed in an oven at 180 °C for 12 h. The following washing and drying process remained unchanged, as described above. Second, a popular surface modification and chemical doping method, cold plasma technique, was applied to treat the $Ti_3C_2$ MXene, which was anhydrous, conducted at low vacuum.[39] The experiment was conducted in a plasma generator device (SAOT YZD08-5C). A similar scheme of the device was shown elsewhere.[40] In this work, the radio frequency (13.56 MHz) was used to generate the plasma, and high pure nitrogen gas ($N_2$) was selected to be the precursor (nitrogen source). The working vacuum was generally 60 Pa, with a treatment time of 10 min. Finally, the $Ti_3CN$ MXene, with the nitrogen element doubtlessly distributed at the lattice site, was synthesized by etching from its precursor $Ti_3AlCN$ phase. A detailed description on the synthesis of $Ti_3CN$ MXene can be found elsewhere.[41]

*DFT Simulation*: The modeling in this work was carried out using the Vienna Ab initio Simulation Package (VASP) in the framework of the DFT. The projector augmented wave (PAW) method was adopted to solve the Kohn–Sham equations,[42] and the generalized gradient approximation constructed by Perdew–Burke–Ernzerhof (GGA-PBE) was selected to describe the exchange–correlation functional.[43] The unitcell of $Ti_3C_2T_2$ (T = F, OH, and O) was first optimized, and then a $3 \times 3 \times 1$ supercell was constructed to accommodate the nitrogen dopant, based on which the defect formation energy and electronic properties were calculated. In order to sample the $k$-space within the Brillouin zone, the Γ centered Monkhorst–Pack grids were used,[44] and the total number of the $k$-points was set to be 40, along with a plane-wave cutoff energy of 480 eV, which made the accuracy within 1 meV per atom. Similar calculation parameters were adopted in some other literature as well.[20,45]

*Material Characterization*: The morphology of the obtained MXene powders was observed using an SEM (FEI Quanta 3D FEG), equipped with an EDS (Oxford X-Max 50) system for chemical composition analysis. To determine the existing form of nitrogen dopants in MXene, XPS (Thermo Escalab 250XI) measurements were conducted with an exciting source of Al K$\alpha$ radiation. In addition, XRD (SmartLab-3) investigation was performed to determine the interlayer spacing of the four MXenes, with Cu K$\alpha$ radiation at a scanning step of 0.05 and a scanning rate of 5° $min^{-1}$. The Raman spectra were collected from a LabRam HR Evolution (Horiba) Raman spectrometer using the second harmonic ($\lambda = 532$ nm) of a pulsed Nd:YAG laser.

*Electrochemical Tests*: The electrochemical measurements in this work were carried out on a CHI 660E workstation (CH Instruments) using a traditional three-electrode setup in 6 м KOH aqueous electrolyte, with a platinum plate ($1 \times 1$ $cm^2$) as the counter electrode, Hg/HgO as the reference electrode, and MXene-based active material as the working electrode. The working electrode was prepared by smearing the mixture of polyvinylidene fluoride (PVDF), acetylene black, and MXene at the ratio of 1:1:8, then dispersed in *N*-methyl pyrrolidone (NMP) onto a piece of nickel foam, followed by a drying process at 80 °C for 12 h in a vacuum oven. Loading mass of the active material on each current collector was around 2 mg. Afterward, the electrochemical performance of the MXenes was measured. CV was tested at the scan rates of 5, 20, 50, and 100 mV $s^{-1}$, and then the specific capacitance ($C_s$) could be calculated according to $C_s = \frac{1}{2ms\Delta V} \int I dV$, where $m$ is the mass of the electroactive material, $s$ is the scan rate, $\Delta V$ is the potential window, and $I$ is the current load.[46] Finally, the electrochemical impedance spectroscopy (EIS) was obtained in the frequency ranging from $10^{-2}$ to $10^5$ Hz within a 5 mV amplitude at open circuit voltage.

## Supporting Information

Supporting Information is available from the Wiley Online Library or from the author.

ADVANCED
SCIENCE NEWS
www.advancedsciencenews.com

ADVANCED
FUNCTIONAL
MATERIALS
www.afm-journal.de

## Conflict of Interest

The authors declare no conflict of interest.

[1] a) K. Gopalakrishnan, A. Govindaraj, C. N. R. Rao, *J. Mater. Chem. A* **2013**, *1*, 7563; b) S. M. Li, S. Y. Yang, Y. S. Wang, H. P. Tsai, H. W. Tien, S. T. Hsiao, W. H. Liao, C. L. Chang, C. C. M. Ma, C. C. Hu, *J. Power Sources* **2015**, *278*, 218.

[2] a) J. Zhang, W. Z. Ma, Z. Y. Feng, F. F. Wu, D. H. Wei, B. J. Xi, S. L. Xiong, *J. Energy Chem.* **2019**, *39*, 54; b) A. Hosseinian, S. Soleimani-amiri, S. Arshadi, E. Vessally, L. Edjlali, *Phys. Lett. A* **2017**, *381*, 2010.

[3] a) Y. Lei, K. Fujisawa, F. Zhang, N. Briggs, A. R. Aref, Y. T. Yeh, Z. Lin, J. A. Robinson, R. Rajagopalan, M. Terrones, *ACS Appl. Energy Mater.* **2019**, *2*, 8625; b) J. C. Wang, L. Y. Zhang, K. Sun, J. J. He, Y. J. Zheng, C. H. Xu, Y. X. Zhang, Y. Chen, M. Li, *Chem. Eng. J.* **2019**, *372*, 665.

[4] M. Kaur, M. Kaur, V. K. Sharma, *Adv. Colloid Interface Sci.* **2018**, *259*, 44.

[5] T. Lin, I. W. Chen, F. Liu, C. Yang, H. Bi, F. Xu, F. Huang, *Science* **2015**, *350*, 1508.

[6] E. J. Biddinger, D. von Deak, U. S. Ozkan, *Top. Catal.* **2009**, *52*, 1566.

[7] H. T. Larijani, M. Khorshidian, *Appl. Surf. Sci.* **2019**, *492*, 826.

[8] H. B. Wang, T. Maiyalagan, X. Wang, *ACS Catal.* **2012**, *2*, 781.

[9] Z. Jin, J. Yao, C. Kittrell, J. M. Tour, *ACS Nano* **2011**, *5*, 4112.

[10] H. L. Guo, Q. M. Gao, *J. Power Sources* **2009**, *186*, 551.

[11] M. Naguib, M. Kurtoglu, V. Presser, J. Lu, J. J. Niu, M. Heon, L. Hultman, Y. Gogotsi, M. W. Barsoum, *Adv. Mater.* **2011**, *23*, 4248.

[12] a) M. R. Lukatskaya, O. Mashtalir, C. E. Ren, Y. Dall'Agnese, P. Rozier, P. L. Taberna, M. Naguib, P. Simon, M. W. Barsoum, Y. Gogotsi, *Science* **2013**, *341*, 1502; b) M. Naguib, V. N. Mochalin, M. W. Barsoum, Y. Gogotsi, *Adv. Mater.* **2014**, *26*, 992; c) M. Naguib, O. Mashtalir, J. Carle, V. Presser, J. Lu, L. Hultman, Y. Gogotsi, M. W. Barsoum, *ACS Nano* **2012**, *6*, 1322.

[13] C. H. Yang, Y. Tang, Y. P. Tian, Y. Y. Luo, Y. C. He, X. T. Yin, W. X. Que, *Adv. Funct. Mater.* **2018**, *28*, 11.

[14] J. B. Pang, R. G. Mendes, A. Bachmatiuk, L. Zhao, H. Q. Ta, T. Gemming, H. Liu, Z. F. Liu, M. H. Rummeli, *Chem. Soc. Rev.* **2019**, *48*, 72.

[15] a) Y. Dall'Agnese, M. R. Lukatskaya, K. M. Cook, P. L. Taberna, Y. Gogotsi, P. Simon, *Electrochem. Commun.* **2014**, *48*, 118; b) Z. Ling, C. E. Ren, M. Q. Zhao, J. Yang, J. M. Giammarco, J. Qiu, M. W. Barsoum, Y. Gogotsi, *Proc. Natl. Acad. Sci. USA* **2014**, *111*, 16676.

[16] W. Z. Bao, L. Liu, C. Y. Wang, S. Choi, D. Wang, G. X. Wang, *Adv. Energy Mater.* **2018**, *8*, 1702485.

[17] a) C. H. Yang, W. X. Que, Y. Tang, Y. P. Tian, X. T. Yin, *J. Electrochem. Soc.* **2017**, *164*, A1939; b) Q. Pang, J. Tang, H. Huang, X. Liang, C. Hart, K. C. Tam, L. F. Nazar, *Adv. Mater.* **2015**, *27*, 6021.

[18] Y. Y. Wen, T. E. Rufford, X. Z. Chen, N. Li, M. Q. Lyu, L. M. Dai, L. Z. Wang, *Nano Energy* **2017**, *38*, 368.

[19] Y. P. Tian, W. X. Que, Y. Y. Luo, C. H. Yang, X. T. Yin, L. B. Kong, *J. Mater. Chem. A* **2019**, *7*, 5416.

[20] Q. Xu, L. Ding, Y. Y. Wen, W. J. Yang, H. J. Zhou, X. Z. Chen, J. Street, A. G. Zhou, W. J. Ong, N. Li, *J. Mater. Chem. C* **2018**, *6*, 6360.

[21] C. H. Yang, Y. Tang, Y. P. Tian, Y. Y. Luo, M. F. U. Din, X. T. Yin, W. X. Que, *Adv. Energy Mater.* **2018**, *8*, 1802087.

[22] a) X. Z. Chen, Z. Z. Kong, N. Li, X. J. Zhao, C. H. Sun, *Phys. Chem. Chem. Phys.* **2016**, *18*, 32937; b) D. Wang, Y. Gao, Y. Liu, D. Jin, Y. Gogotsi, X. Meng, F. Du, G. Chen, Y. Wei, *J. Phys. Chem. C* **2017**, *121*, 13025.

[23] O. Mashtalir, M. Naguib, V. N. Mochalin, Y. Dall'Agnese, M. Heon, M. W. Barsoum, Y. Gogotsi, *Nat. Commun.* **2013**, *4*, 1716.

[24] A. N. Enyashin, A. L. Ivanovskii, *J. Solid State Chem.* **2013**, *207*, 42.

[25] M. Naguib, O. Mashtalir, M. R. Lukatskaya, B. Dyatkin, C. Zhang, V. Presser, Y. Gogotsi, M. W. Barsoum, *Chem. Commun.* **2014**, *50*, 7420.

[26] A. C. Ferrari, J. Robertson, *Phys. Rev. B* **2000**, *61*, 14095.

[27] Y. Tang, J. F. Zhu, W. L. Wu, C. H. Yang, W. J. Lv, F. Wang, *J. Electrochem. Soc.* **2017**, *164*, A923.

[28] a) A. M. Jastrzebska, A. Szuplewska, T. Wojciechowski, M. Chudy, W. Ziemkowska, L. Chlubny, A. Rozmyslowska, A. Olszyna, *J. Hazard. Mater.* **2017**, *339*, 1; b) A. Rozmyslowska-Wojciechowska, T. Wojciechowski, W. Ziemkowska, L. Chlubny, A. Olszyna, A. M. Jastrzebska, *Appl. Surf. Sci.* **2019**, *473*, 409.

[29] M. M. Hu, Z. J. Li, T. Hu, S. H. Zhu, C. Zhang, X. H. Wang, *ACS Nano* **2016**, *10*, 11344.

[30] Y. Yoon, M. Lee, S. K. Kim, G. Bae, W. Song, S. Myung, J. Lim, S. S. Lee, T. Zyung, K. S. An, *Adv. Energy Mater.* **2018**, *8*, 11.

[31] M. R. Lukatskaya, S. M. Bak, X. Q. Yu, X. Q. Yang, M. W. Barsoum, Y. Gogotsi, *Adv. Energy Mater.* **2015**, *5*, 1500589.

[32] X. P. Mu, D. S. Wang, F. Du, G. Chen, C. Z. Wang, Y. J. Wei, Y. Gogotsi, Y. Gao, Y. Dall'Agnese, *Adv. Funct. Mater.* **2019**, *29*, 1902953.

[33] a) B. Yan, C. Lu, P. Zhang, J. Chen, W. He, W. Tian, W. Zhang, Z. Sun, *Mater. Today Commun.* **2020**, *22*, 100713; b) Y. Jiang, T. Sun, X. Xie, W. Jiang, J. Li, B. Tian, C. Su, *ChemSusChem* **2019**, *12*, 1368.

[34] R. T. Wang, S. J. Wang, Y. B. Zhang, D. D. Jin, X. Y. Tao, L. Zhang, *J. Mater. Chem. A* **2018**, *6*, 1017.

[35] L. F. Chen, X. D. Zhang, H. W. Liang, M. Kong, Q. F. Guan, P. Chen, Z. Y. Wu, S. H. Yu, *ACS Nano* **2012**, *6*, 7092.

[36] X. Du, C. Y. Wang, M. M. Chen, Y. Jiao, J. Wang, *J. Phys. Chem. C* **2009**, *113*, 2643.

[37] J. G. Wang, Y. Yang, Z. H. Huang, F. Y. Kang, *J. Power Sources* **2013**, *224*, 86.

[38] L. Yang, W. Zheng, P. Zhang, J. Chen, W. Zhang, W. B. Tian, Z. M. Sun, *Electrochim. Acta* **2019**, *300*, 349.

[39] Z. Han, A. T. Murdock, M. Seo, A. Bendavid, *2D Mater.* **2018**, *5*, 032002.

[40] Y. Y. Hsieh, L. Zhang, D. DeArmond, S. N. Kanakaraj, P. K. Adusei, N. T. Alvarez, Y. B. Fang, J. Daum, V. Shanov, *Carbon* **2018**, *139*, 1093.

[41] K. Hantanasirisakul, M. Alhabeb, A. Lipatov, K. Maleski, B. Anasori, P. Salles, C. Ieosakulrat, P. Pakawatpanurut, A. Sinitskii, S. J. May, Y. Gogotsi, *Chem. Mater.* **2019**, *31*, 2941.

[42] P. E. Blöchl, *Phys. Rev. B* **1994**, *50*, 17953.

[43] J. P. Perdew, K. Burke, M. Ernzerhof, *Phys. Rev. Lett.* **1996**, *77*, 3865.

[44] H. J. Monkhorst, J. D. Pack, *Phys. Rev. B* **1976**, *13*, 5188.

[45] Q. Tang, Z. Zhou, P. Shen, *J. Am. Chem. Soc.* **2012**, *134*, 16909.

[46] A. Amiri, Y. Chen, C. B. Teng, M. Naraghi, *Energy Storage Mater.* **2020**, *25*, 731.